The Astrophysical Journal, 760:140 (16pp), 2012 December 1 doi:10.1088/0004-637X/760/2/140

RE-EVALUATING WASP-12b: STRONG EMISSION AT 2.315 μm, DEEPER OCCULTATIONS, AND AN ISOTHERMAL ATMOSPHERE

Ian J. M. Crossfield[1,2], Travis Barman[3], Brad M. S. Hansen[2], Ichi Tanaka[4], and Tadayuki Kodama[4]
[1] Max-Planck Institüt für Astronomie, Königstuhl 17, D-69117 Heidelberg, Germany; ianc@mpia.de
[2] Department of Physics & Astronomy, University of California Los Angeles, Los Angeles, CA 90095, USA
[3] Lowell Observatory, 1400 West Mars Hill Road, Flagstaff, AZ 86001, USA
[4] Subaru Telescope, National Astronomical Observatory of Japan, 650 North A'ohoku Place, Hilo, HI 96720, USA
Received 2012 July 17; accepted 2012 October 16; published 2012 November 16

ABSTRACT

We revisit the atmospheric properties of the extremely hot Jupiter WASP-12b in light of several new developments. First, we present new narrowband (2.315 μm) secondary eclipse photometry, which exhibits a planet/star flux ratio of 0.45% $\pm$ 0.06%, corresponding to a brightness temperature of 3640 $\pm$ 230 K; second, recent *Spitzer*/Infrared Array Camera and *Hubble Space Telescope*/Wide Field Camera 3 observations; and third, a recently observed star only 1″ from WASP-12, which has diluted previous observations and which we further characterize here. We correct past WASP-12b eclipse measurements for the presence of this object, and we revisit the interpretation of WASP-12b's dilution-corrected emission spectrum. The resulting planetary emission spectrum is well approximated by a blackbody, and consequently our primary conclusion is that the planet's infrared photosphere is nearly isothermal. Thus, secondary eclipse spectroscopy is relatively ill suited to constrain WASP-12b's atmospheric abundances, and transmission spectroscopy may be necessary to achieve this goal.

Key words: eclipses – infrared: planetary systems – stars: individual (WASP-12, Bergfors-6) – techniques: photometric – techniques: spectroscopic

Online-only material: color figures

1. INTRODUCTION

Transiting extrasolar planets allow the exciting possibility of studying the intrinsic physical properties of these planets. The latest new frontier to emerge is the detailed study of molecular chemistry in the atmospheres of these planets, many of which exist in intensely irradiated environments. Recent years have seen rapid strides in this direction, with measurements of precise masses and radii, detection of secondary eclipses and phase curves, and the start of ground-based spectroscopy (Redfield et al. 2008; Swain et al. 2010; Bean et al. 2010). Based on observed day/night temperature contrasts (e.g., Cowan & Agol 2011), atmospheric circulation patterns (Knutson et al. 2009), and atmospheric chemistry (Stevenson et al. 2010; Madhusudhan et al. 2011), these planets' atmospheres are likely to be quite different from anything previously known.

1.1. Introducing the WASP-12 System

A prime example is the transiting Hot Jupiter WASP-12b, which is one of the largest and hottest transiting planets known (Hebb et al. 2009; Chan et al. 2011; Maciejewski et al. 2011). The planet is significantly overinflated as compared to standard interior models (Fortney et al. 2007), though its radius and age can be explained by an appropriate dynamical history involving an initially eccentric orbit and subsequent interior dissipation of tidal torques (Ibgui et al. 2011). Radial velocity measurements associated with the initial transit discovery and the first occultation observation both suggested that WASP-12b had a nonzero eccentricity (Hebb et al. 2009; López-Morales et al. 2010). However, subsequent orbital characterization via timing of secondary eclipses (Croll et al. 2011; Campo et al. 2011; Cowan et al. 2012) and further radial velocity measurements (Husnoo et al. 2011) set an upper limit on the eccentricity of $\sim$0.03(1σ). The 2.315 μm narrowband eclipse we present here is also consistent with a circular orbit.

Due to its close proximity to its host star, the planet is thought to be significantly distorted and may even be undergoing Roche lobe overflow (Li et al. 2010). Such overflow, if verified, would be the first evidence of the tidal inflation instability (Gu et al. 2003). Possible evidence for the overflow scenario has come from (1) *Hubble Space Telescope* (*HST*)/Cosmic Origins Spectrograph (COS) UV spectra taken during transit (Fossati et al. 2010), which show tentative evidence of a deeper transit with earlier ingress than observed in the optical (Hebb et al. 2009), (2) a tentative detection of an extended Ks-band secondary eclipse duration (Croll et al. 2011), which could be interpreted as an opaque accretion stream or disk, and (3) *Spitzer*/Infrared Array Camera (IRAC) phase curve observations of WASP-12b, which detect ellipsoidal variations from the planet at 4.5 μm at a level consistent with a planet filling (or overfilling) its Roche lobe (Cowan et al. 2012). However, (1) there is no evidence for an extended occultation duration in *Spitzer*/IRAC observations (Campo et al. 2011) or in the 2.315 μm narrowband eclipse we present here; (2) degeneracies between ellipsoidal variations, thermal phase variations, and instrumental systematics prevent an unambiguous determination of WASP-12b's geometry from the *Spitzer* observations (Cowan et al. 2012); and (3) recent *HST*/Wide Field Camera 3 (WFC3) secondary eclipse spectroscopy suggests that WASP-12b is not substantially distorted (Swain et al. 2012).

WASP-12b is intensely irradiated by its host star, making the planet one of the hottest known and giving it a favorable ($\gtrsim 10^{-3}$) near-infrared (NIR) planet/star flux contrast ratio; its atmosphere has quickly become one of the best studied outside the solar system. The planet's large size, low density, and high temperature motivated a flurry of optical (López-Morales et al. 2010), NIR (Croll et al. 2011), and mid-infrared

(MIR; Campo et al. 2011) secondary eclipse photometry and has been interpreted to reflect an atmosphere with an unusual carbon-to-oxygen ratio (C/O) greater than 1 (Madhusudhan et al. 2011). Subsequent ground-based observations (Zhao et al. 2012; Crossfield et al. 2012) and the recent WFC3 1.1–1.7 μm spectrum (Swain et al. 2012) are consistent with these earlier measurements and the C/O $>$ 1 model, but the 2.315 μm eclipse we present here is inconsistent (at $>3\sigma$) with such models. In addition, under the so-called null hypothesis (i.e., a spherical planet) of Cowan et al. (2012) the IRAC 4.5 μm secondary eclipse is significantly deeper than the previous measurement (Campo et al. 2011), suggesting less absorption by CO and weakening the case for a high C/O.

As yet transmission spectroscopy (which determines atmospheric opacity at a planet's limb via multi-wavelength transit measurements; Seager & Sasselov 2000) has so far been limited for this system. Optical transit measurements show some disagreement (Hebb et al. 2009; Chan et al. 2011; Maciejewski et al. 2011), which makes interpretation difficult. *Spitzer*/IRAC transit observations suggest that WASP-12b's radius may be greater at 3.6 μm than at 4.5 μm (Cowan et al. 2012), but only if the planet is much more prolate ($R_{\rm long}/R_p = 1.8$) than suggested by WFC3 observations (3σ upper limit of 1.7; Swain et al. 2012). Under the null hypothesis of Cowan et al. (2012), the transit radius is larger at 4.5 μm (as expected from atmospheric models). WASP-12b's low density and high temperature ensure that this planet will continue to be a target for future efforts in this direction; if (as we suggest) the planet's atmosphere is in fact nearly isothermal at the pressures probed in secondary eclipse, transmission spectroscopy may be the only hope for constraining WASP-12b's atmospheric composition.

Thus, significant uncertainties remain in the interpretation of the current ensemble of atmospheric measurements. At the moment, this situation is typical even for the best-characterized systems (Madhusudhan & Seager 2010) because (1) broadband photometry averages over features caused by separate opacity sources and (2) atmospheric models have many more free parameters than there are observational constraints. When properly calibrated, spectrally resolved measurements can break some of these degeneracies. Such results can test the interpretation of photometric observations at higher resolution, and can more precisely refine estimates of atmospheric abundances, constrain planetary temperature structures, and provide deeper insight into high-temperature exoplanetary atmospheres. These goals provided the motivation for our earlier ground-based spectroscopy of WASP-12b (Crossfield et al. 2011) and serve as the impetus for the analysis presented here.

1.2. Paper Outline

This paper presents new secondary eclipse observations of WASP-12b's emission in a narrow band centered at 2.315 μm, our detection and characterization of a cool star (which we call Bergfors-6) with high surface gravity near WASP-12, a correction of past eclipse measurements for the dilution caused by Bergfors-6, and our interpretation of WASP-12b's atmospheric emission.

We describe our secondary eclipse observations and initial data reduction in Section 2. As described in Section 3, we fit numerous model light curves to the data, select the statistically optimal combination of parameters to use, and present the results of this eclipse. In Section 4 we describe our analysis of Bergfors-6's properties, and in Section 5 we use the results of this analysis to correct past transits and occultations of WASP-12b. In Section 6, we discuss our analysis of WASP-12b's corrected emission spectrum and provide updated constraints on the planet's bolometric luminosity. Finally, we conclude and suggest relevant possibilities for follow-up in Section 7.

2. SUBARU/MOIRCS NARROWBAND TIME-SERIES PHOTOMETRY

2.1. Summary of Observations

We recently described the first tentative detection of emission from WASP-12b via spectroscopy at the 3 m NASA Infrared Telescope Facility (IRTF; Crossfield et al. 2012). However, our precision was strongly limited by chromatic and time-dependent slit losses resulting from the use of a single, narrow (3″) slit. We subsequently obtained time on the Multi-Object Infrared Camera and Spectrograph (MOIRCS; Ichikawa et al. 2006; Suzuki et al. 2008) at Subaru Observatory to conduct multi-object occultation spectroscopy of WASP-12b. A coolant leak at Subaru caused damage that prevented us from obtaining spectroscopy, so we operated the instrument in an imaging mode using a custom narrowband filter. This filter (NB2315) is centered at approximately 2.315 μm with a width at half-maximum of 27 nm,[5] and so is very well suited to probe the strong absorption feature predicted to lie at this wavelength by models used to infer a high C/O (Madhusudhan et al. 2011, their Figure 1).

We observed one secondary eclipse of WASP-12b on UT 2011 December 14. The start of observations was delayed by instrument problems, but we managed to begin about half an hour before ingress and observed continuously thereafter. We observed at a position angle of 330° and read out frames in a correlated double sampling (CDS) mode with a constant integration time of 21 s per frame, using a readout speed of 8 and two dummy reads (this last choice suppresses a known, variable-bias effect; Katsuno et al. 2003). These readout parameters result in substantial overhead penalties, and we averaged only one frame per 61 s over our 6.5 hr of observations (which cover an airmass range of 1.6–1.02–1.3). We recorded 388 frames in total. Conditions were nearly photometric, with stellar flux variations of 1%–2% apparent.

Following standard practices for high-precision photometry (e.g., de Mooij & Snellen 2009; Rogers et al. 2009), we defocused the telescope to spread the starlight over more pixels, thereby increasing observing efficiency and reducing the effect of residual flat-fielding errors. The instrumental seeing improved throughout the night, and to avoid any substantially nonlinear detector response we added additional defocus to the telescope several times. Because the Subaru autoguider was inoperative we had to periodically apply manual offsets to the telescope tracking. The tracking was rather poor and despite our corrections we observed image drifts as large as 1.″2 (10 pixels); however, subsequent software development at Subaru has improved the tracking in the absence of the autoguider. The temperature of both detectors (as reported by the `CHIPBOX` FITS header keywords) increased from 76.2 K to a constant 77.0 K over the first 1.5–2 hr. All these instrumental trends are shown in Figure 1, but we ultimately find that they do not significantly affect our photometry.

[5] A transmission profile of the NB2315 filter is available upon request from T.K.

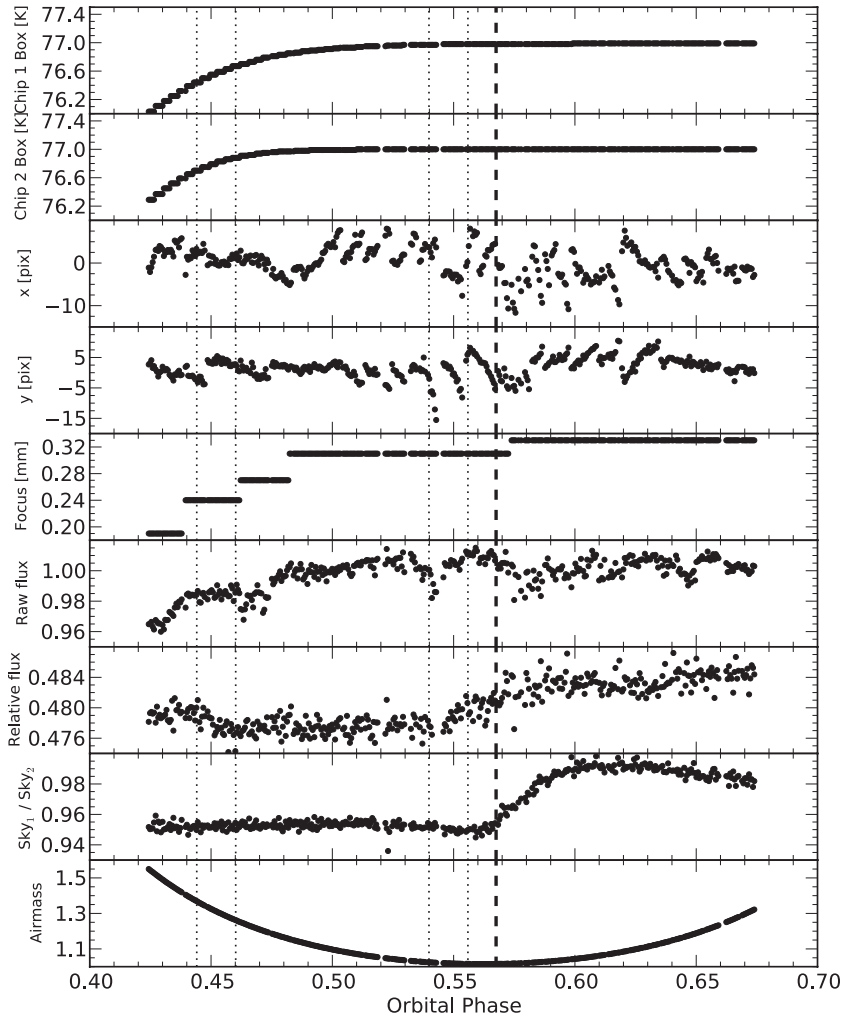

Figure 1. Instrumental trends during our observations. From top to bottom: Chips 1 and 2 electronics box temperatures, relative x and y motions, telescope focus encoder setting, WASP-12 raw flux, WASP-12 relative flux, ratio of median sky background (pre-calibration) in Chips 1 and 2, and airmass. The dotted lines indicate the four points of contact corresponding to a circular orbit with our best-fit secondary eclipse center. The vertical dashed line corresponds to the onset of the anomalous trend apparent in the sky background and relative photometry: we exclude all data after this in our final analysis.

2.2. Initial Data Reduction

MOIRCS splits its field of view across two detectors, and we reduce the data from each detector independently. We calibrate the raw frames following the standard MOIRCS reduction prescription, which proceeds as follows. MOIRCS returns the UT date and time at the beginning and end of each exposure in its FITS header. We convert these to $\mathrm{BJD_{TDB}}$ for our subsequent analysis (Eastman et al. 2010). We dark-subtract each frame and divide the result by the stack median of a set of dark-subtracted dome flats. Next, we correct our data for the intrinsic nonlinearity of infrared detector arrays (Vacca et al. 2004).[6] Using a set of flat frames taken with typical counts ranging from 2000 to 22,000 ADU, we compute the median linearity correction coefficients $(a_1, \ldots, a_4)$ of Vacca et al.'s (2004) Equation (20):

$$C_{nl} = (1 + a_1 x + a_2 x^2 + a_3 x^3 + a_4 x^4)^{-1} \quad (1)$$

(where C_{nl} is the ratio of an ideally linear signal to the measured signal) to be

$$a_1, a_2, a_3, a_4 = (0.00347574, -0.00436064, -0.00111471, 0.00048908)$$

for Chip 1, and

$$a_1, a_2, a_3, a_4 = (0.0063929, -0.0139614, 0.00548463, -0.00081818)$$

for Chip 2. We define x as the measured ADU counts divided by 10^4 to avoid very small coefficients. We then iteratively apply the correction algorithm in Vacca et al.'s Equations (21)–(26), while further requiring that C_{nl} is always $\geqslant 1$. Convergence typically occurs within four to five iterations. The nonlinearity correction is critical in our analysis: it changes our relative photometry by as much as 0.5% in some frames, and it slightly reduces our final, residual photometric root mean square (RMS) from 0.234% to 0.232%.

At this point in the analysis substantial scattered and/or background light remains: we remove this by scaling and subtracting

[6] A Python implementation of our MOIRCS nonlinearity correction algorithm is available from the primary author's Web site.

a median-combined set of median-normalized, dithered, dark-subtracted sky images. We follow these procedures independently for data from both channels; requiring an identical level of sky subtraction in both channels does not significantly change our results.

We extract photometry using our own aperture photometry package,[7] which uses bilinear interpolation to account for partial pixels while conserving flux. In each frame we extract subregions around each star, perform one-dimensional cross-correlations to measure relative stellar motions, and interpolate over hot pixels, stuck pixels, and any pixels more than 6σ discrepant from their mean value. We then recenter the photometric apertures and perform standard aperture photometry.

In its imaging mode, MOIRCS offers a roughly $4' \times 7'$ field of view split equally over two 2048^2 HAWAII-2 detectors, which allows several comparison stars to be fit into the WASP-12 field of view. Using stars more than about 1.8 mag fainter than WASP-12 decreases our final precision. Our large photometric apertures also require us to avoid choosing comparison stars with nearby companions. This leaves five comparison stars: 2MASS stars 06302437+2937293 and 06303222+2937347 (on Chip 1) and 06302377+2939118, 06301801+2939204, and 06302280+2938338 (WASP-12 is on Chip 2). Our final results are consistent (though of lower precision) if we use fewer comparison stars or use comparison stars falling only on a single detector. We examine the results from photometric apertures of various sizes and ultimately use target and inner and outer sky apertures with diameters of 39, 47, and 72 pixels ($4\farcs6$, $5\farcs5$, and $8\farcs4$, respectively). This choice minimizes the RMS of the residuals to our model fits; the final RMS is 0.232%.

2.3. Instrumental Systematics

We plot several variable instrumental parameters, along with the absolute and relative photometry of WASP-12, in Figure 1. One variable dominates in terms of its impact on our photometry: the curious trend in the ratio of the median sky background measured in the two detectors, which begins an anomalous excursion as WASP-12 crosses the meridian (only 10–15 minutes after egress) before later stabilizing at a new level. The relative photometry shows a qualitatively similar trend superimposed on a secondary eclipse (visible in the raw data).

We also see this trend when dividing stellar photometry from Chip 2 (excluding WASP-12) by photometry from Chip 1, and we even see it (at a lower amplitude) when comparing multiple reference stars on Chip 2 against each other; it is thus a field-dependent effect. Because the trend begins just as WASP-12 crosses the meridian, we hypothesize that some loose component in the telescope or instrument settled in response to the change in the direction of the gravity vector.

One possible culprit in this scenario is our narrowband filter, whose spectral transmission profile depends on the angle of incidence of incoming light. To first order, increasing the angle of incidence translates the transmission profile to shorter wavelengths. The filter profile intersects a particularly strong telluric absorption (CH_4) band head; from the vendor-supplied characterization data for our filter, we estimate that a shift in the filter's angle of incidence of $\sim 10^\circ$ could induce a photometric variation of the magnitude observed. However, no strong sky emission features are seen at these wavelengths, so this scenario still has difficulty explaining the observed variation in the sky background. Regardless, subsequent MOIRCS multi-object spectroscopic data do not show this anomalous trend, a fact consistent with our hypothesis that the trend's presence is somehow related to the NB2315 filter.

Whatever the cause of this anomalous trend, so long as we restrict our analysis to times before orbital phase 0.5675 (the vertical dashed bar in Figure 1), our results change by less than 1.5σ no matter which comparison stars we choose. This choice leaves pre- and post-eclipse baselines which are rather short. We explored ways to use our entire data set by using the sky-background trend as a decorrelation parameter (see Section 3), but such analyses resulted in larger fit residuals with substantially higher correlations on long timescales. We therefore proceed by excluding the later data, while acknowledging the existence of this poorly understood systematic effect in MOIRCS narrowband imaging data.

3. 2.315 μm NARROWBAND SECONDARY ECLIPSE

We now present our analysis of the narrowband photometry discussed in the preceding section. In Section 3.1, we describe the process of selecting an optimal model for our data and fitting this model to the data. In Section 3.2, we describe the primary result of the fitting process: a 2.315 μm eclipse depth significantly discrepant from previous predictions. Then in Section 3.3 we show that the occultation we detect has a duration and time of center consistent with that expected for WASP-12b on a circular orbit.

3.1. Fitting to the Data

We fit our photometric time series with the following relation, representing a relative secondary eclipse light curve subjected to systematic effects:

$$F_i = f_0 (1 + d\ell_i) \left(1 + \sum_{j=1}^{J} c_j v_{ij} \right). \quad (2)$$

The symbols are defined as follows: F_i, the relative flux measured at time step i; f_0, the true relative flux; ℓ_i, the flux in an occultation light curve scaled to equal zero out of eclipse and -1 inside eclipse; d, the normalized depth of secondary eclipse; v_{ij}, the J state vectors (i.e., image motions, sky background, airmass, orbital phase, or low-order polynomials of these quantities) exhibiting a linearly perturbative effect on the instrumental sensitivity; and c_j, the coefficients for each state vector.

Experience shows that the choice of instrumental model is of crucial importance in extracting the most accurate system parameters from transit and occultation observations (e.g., Campo et al. 2011). We therefore explore a large region of model parameter space by fitting our photometry using many different combinations of state vectors and a fixed secondary eclipse time and duration. We then use the Bayesian Information Criterion (BIC[8]) to choose which of these many models best represents our data. To do this we first assign uncertainties to each data point equal to the RMS of the residuals to an eclipse fit with no additional decorrelation variables. We find that the BIC-minimizing model includes a transit light curve and a linear function of time, but no additional parameters. The model with the next best BIC (3.2 units higher) also includes a linear function of the x position of the stars on the detector; both

[7] Available from the primary author's Web site.

[8] $\mathrm{BIC} = \chi^2 + k \ln N$, where k is the number of free parameters and N is the number of data points.

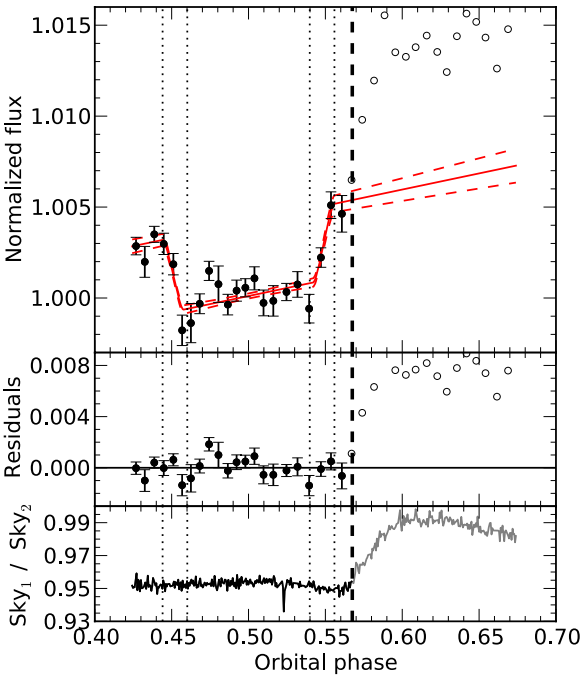

Figure 2. Top: relative 2.315 μm narrowband photometry of WASP-12 (points, binned by a factor of 10 for plotting purposes; error bars are the standard deviation on the mean of each set of 10 points) and our best-fit model (solid line). The 1σ range of our model is also indicated by the dashed curves. Solid points are used in our analysis, while open points are excluded. Middle: residuals to the fit. Bottom: differential sky background measured in the two MOIRCS detectors. The vertical dashed line indicates the onset of the photometric ramp apparent in sky and stellar photometry; we exclude this data from our analysis, though the occultation depth is unchanged if we use all data and include the sky trend as an additional decorrelation parameter. The dotted lines indicate the four points of contact corresponding to a circular orbit with our best-fit eclipse center.

(A color version of this figure is available in the online journal.)

Table 1
WASP-12b: 2.315 μm Narrowband Secondary Eclipse Parameters

Parameter	Units	Value	Reference
P	days	1.091423	Hebb et al. (2009)
a/R_*	...	3.14	Hebb et al. (2009)
$T_{c,e}$	$\mathrm{BJD_{TDB}}$	2455910.9090 ± 0.0013	This work
T_{offset}	s	7 ± 110	This work
T_{58}	minutes	179.6 ± 4.5	This work
$e \cos \omega$	...	$+0.00006 \pm 0.00091$	This work
$e \sin \omega$	...	0.011 ± 0.013	This work
F_P/F_* (observed)	...	$0.47\% \pm 0.05\%$	This work
F_P/F_* (corrected)	...	$0.45\% \pm 0.06\%$	This work
$T_{B,2.315}$	K	3640 ± 230	This work

this model and a model including no decorrelation parameters ($\Delta\mathrm{BIC} = 10.7$) return secondary eclipse depths consistent with that of our optimal model.

We then again fit our preferred instrumental model to the data, but now allowing the secondary eclipse center, duration, and depth to vary while holding fixed the scaled semimajor axis (a/R_*) and the orbital inclination at the values listed in Table 1. We assess the uncertainties on the best-fit parameters using both the Markov Chain Monte Carlo (MCMC) and prayer-bead (as described in Winn et al. 2008, see also Jenkins et al. 2002) approaches. The two sets of parameter distributions are quite consistent, which suggests that correlated noise does not strongly affect our photometry. In both cases the resulting parameter distributions are unimodal, symmetric, approximately normal, and (excepting the standard correlation between occultation depth and baseline flux) uncorrelated. In the following we quote only the MCMC results, which provide substantially denser sampling of the posterior distributions than the prayer-bead results.

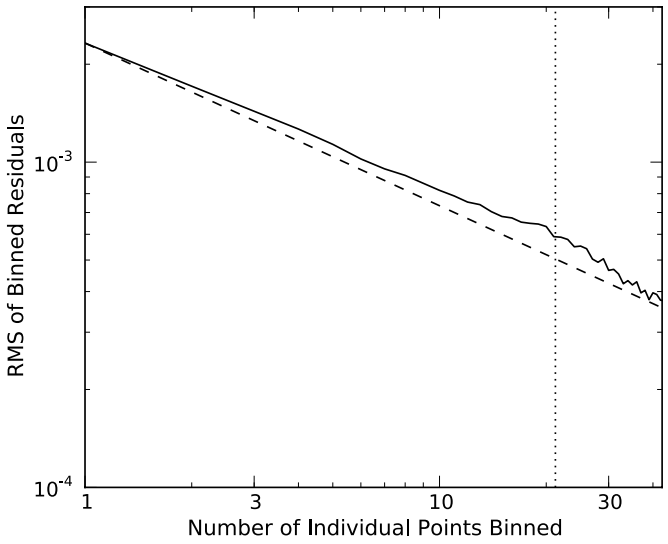

Figure 3. RMS from binning the residuals shown in Figure 2 over increasing numbers of data points (solid black line). This curve exceeds the $N^{-1/2}$ expectation from white noise (dashed line) by increasing amounts on successively longer timescales. The timescale of ingress or egress is indicated by the vertical dotted line.

3.2. Initial Narrowband Eclipse Depth

We plot the data, our best-fit (linear baseline) model, and the residuals in Figure 2. The best-fit secondary eclipse depth is $0.47\% \pm 0.05\%$; note that the true planet/star flux ratio is $\sim$10% greater than this, as we describe in Section 5 and Table 4. We find shallower or deeper best-fit eclipse depths (ranging from roughly 0.41% to 0.50%) when using, respectively, larger or smaller photometric apertures, which indicates the sensitivity of this analysis to our particular choice of parameters. For this reason we quote the measurement uncertainty of 0.05% above, which is roughly twice that predicted from our prayer-bead analysis.

The residuals to the best fit have a relative RMS of 0.232%. Photon (target + sky) noise considerations predict a typical per-frame precision of 0.06%, so our performance is comparable to that obtained with other NIR secondary eclipse photometry (e.g., Croll et al. 2011). Figure 3 shows that our residuals bin down somewhat more slowly than $N^{-1/2}$, indicating a moderate level of correlated residuals.

The largest residuals occur at a "bump" in the light curve at orbital phase 0.47–0.48. One possible explanation is that this excursion is caused by telluric variations that are not entirely common mode across the MOIRCS field of view. An alternate explanation would be a short-term flare from Bergfors-6. We apply Difference Image Analysis (Bramich 2008)[9] to two images generated by co-adding individual frames during and immediately after the bump. The difference image shows no flux excess at the location of Bergfors-6 during this bump, indicating that the residual feature in the time series in not associated with Bergfors-6. More exotic explanations, such as an attribution of

[9] Our Python implementation of this algorithm is available at the primary author's Web site.

this bump to accretion onto WASP-12, should be treated with skepticism at present.

We also attempted an alternative analysis in which we used all the data (including that affected by the anomalous background trend) and included the sky-background trend as an additional decorrelation state vector. This analysis gives a marginally deeper secondary ($0.53\% \pm 0.05\%$), but has a higher residual RMS (0.261%), exhibits substantially higher levels of correlated noise when averaging on long timescales, and shows a significantly nonzero $e\cos\omega$ (inconsistent with previous analysis; cf. Campo et al. 2011; Croll et al. 2011; Cowan et al. 2012). These results suggest that our simpler model, which excludes the latter part of our data set, gives the more reliable occultation measurement.

3.3. Occultation Duration and Timing: No Surprises

We find no evidence for significant deviations in secondary eclipse duration or in the eclipse's time of center as compared to expectations from transit observations and a circular orbit. We find a best-fit eclipse duration of 179.6 ± 4.5 minutes, and the eclipse occurs later than predicted by 7 ± 110 s (after accounting for the 23 s light travel time across the system). Again, the parameter distributions are unimodal and approximately normal. An analysis of previous Ks-band observations reported a marginally longer secondary eclipse duration (195 ± 7 minutes; Croll et al. 2011), while a weighted mean of *Spitzer*/IRAC occultations give a duration of 177.7 ± 2.1 minutes (Campo et al. 2011; Cowan et al. do not report the durations of their transits and eclipses) and the z' occultation showed a duration of 169 minutes (with no uncertainty reported; López-Morales et al. 2010). Our narrowband measurement is consistent with these last two values (and with the duration expected from a circular orbit) and is within 3σ of the Ks-band broadband results. Our data provide no evidence for an offset or longer duration eclipse.

Together, the secondary eclipse timing and duration tightly constrain the orbital eccentricity and longitude of periastron (Winn 2010; Seager 2011). We determine $e\cos\omega$ and $e\sin\omega$ to be $+0.00006 \pm 0.00091$ and 0.011 ± 0.013, respectively, which we interpret as being consistent with a circular orbit and with previous results based on eclipse and radial velocity observations (Campo et al. 2011; Croll et al. 2011; Husnoo et al. 2011). The time of eclipse also constrains the planetary velocity offset expected at transit center, which can mimic wind-induced velocity offsets measured with high-resolution spectroscopy (Snellen et al. 2010; Fortney et al. 2010; Montalto et al. 2011; Miller-Ricci Kempton & Rauscher 2012). Using Equation (3) of Montalto et al. (2011), we set a 3σ upper limit on any such orbit-induced velocity offset of $+0.59$ km s^{-1}.

4. Bergfors-6: AN OBJECT VERY CLOSE TO WASP-12

4.1. Introducing Bergfors-6

Before undertaking an analysis of WASP-12b's atmospheric properties, we first pause to describe our improved characterization of a recently detected point source ~3 mag fainter than WASP-12 and only 1″ away (Bergfors et al. 2011, 2012). This object requires us to revise upward past measurements of the planet's transits and occultations.

During our Subaru observations, one of us (I.T.) noticed a slight elongation in our (defocused) images. This motivated us to refocus the system at the end of the night, and we recorded the image shown in Figure 4. It clearly shows a point source roughly 1″ from WASP-12. A subsequent literature search revealed that this object was recently discovered using i and z photometry and assigned a preliminary spectral type of K4-M1 V (Bergfors et al. 2011, 2012). We refer to this object as Bergfors-6 because it is the sixth object in Table 2 of Bergfors et al. (2012). The existence of a bound companion at this projected separation ($\lesssim$300 AU) would have potentially profound implications for the dynamical history of the system, and could provide a mechanism for Kozai-induced eccentricity and subsequent tidal heating to inflate the planet's radius to its present size (Fabrycky & Tremaine 2007; Nagasawa et al. 2008; Ibgui et al. 2011).

Bergfors-6 has not been remarked upon in previous optical and infrared transit and occultation observations of the WASP-12 system (Hebb et al. 2009; López-Morales et al. 2010; Chan et al. 2011; Maciejewski et al. 2011; Campo et al. 2011; Croll et al. 2011; Cowan et al. 2012; Crossfield et al. 2012; Zhao et al. 2012). This is likely because with seeing-limited or *Spitzer*/IRAC resolution the two objects are at best only marginally resolved. The case is worse for most high-precision ground-based photometry because of the common practice of substantially defocusing the telescope, which will clearly preclude the detection of objects such as Bergfors-6.

This star falls within the photometric apertures used in most previous analyses and dilutes the transit and secondary eclipse signals that have been measured (e.g., Daemgen et al. 2009). In this section, we confirm the previous detection of Bergfors-6 and more tightly constrain its spectral type. In the following section, we then correct previous transit and occultation measurements for the photometric contamination of WASP-12 by Bergfors-6.

4.2. Observations of Bergfors-6

4.2.1. Subaru/MOIRCS NB2315 Image

As described above, we recorded the single well-focused MOIRCS image shown in Figure 4. We register the image's coordinate system using the 2MASS point-source catalog (Skrutskie et al. 2006) and confirm the MOIRCS plate scale to be $0\farcs117 \pm 0\farcs001$ pixel^{-1} (as listed in the instrument documentation). We conservatively adopt an uncertainty of 1° in the instrumental position angle.

Bergfors-6 sits in the wings of the WASP-12 point-spread function (PSF), so we perform a simultaneous fit to the two-dimensional PSFs of both stars. We use multiple elliptical Gaussian functions, holding the rotation and dispersion parameters fixed in each of the model PSFs and allowing only a single central location for each star. Thus, for n Gaussian functions we have $(5 + 5n)$ free parameters. We set the pixel uncertainties equal to the expectation from photon and read noise.

We find that three elliptical Gaussians minimize the BIC, so we adopt this model and use MCMC techniques to explore the range of valid parameter space. We find the subsequent parameter distributions to be unimodal and approximately Gaussian. To conservatively account for the uncertainties inherent in estimating accurate photometry and astrometry from a single frame, we inflate the parameter uncertainties estimated from our MCMC by a factor of two. Our final determination of the flux ratio, separation, and system position angle from the MOIRCS data is listed in Table 2. The astrometry is consistent with the initial discovery values (Bergfors et al. 2011, 2012). We confirm this 2.315 μm flux ratio by comparing aperture photometry of WASP-12 and (after subtraction of the best-fit WASP-12 PSF model) Bergfors-6: this approach gives a consistent result. The measurements presented here are consistent with, but more

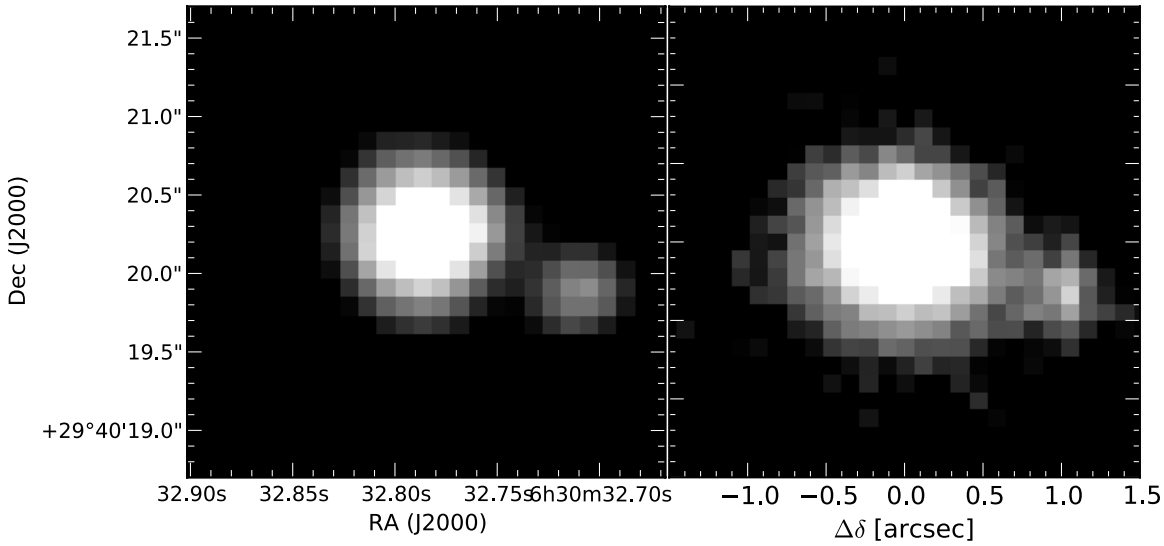

Figure 4. Images used for astrometric and relative flux measurements: at left, seeing-limited image from Subaru/MOIRCS (2.315 μm narrowband); at right, speckle image from IRTF/SpeX ($K_{\rm MKO}$). Astrometric parameters derived from these images are listed in Table 2. Both images are displayed at the same orientation and scale; they have different (logarithmic) color stretches in order to highlight the fainter companion.

Table 2
WASP12/Bergfors-6 Astrometry

Parameter	Units	Subaru/MOIRCS	IRTF/SpeX
Filter	...	NB2315	$K_{\rm MKO}$
Flux ratio	...	0.108 ± 0.007	0.1048 ± 0.0059
Separation	arcsec	1.055 ± 0.026	1.078 ± 0.033
Position angle	deg	250 ± 1	249.4 ± 1.1
Date	UT	2011 Dec 14	2012 Feb 25

Table 3
IRTF/SpeX Astrometric Calibrators[a]

WDS Identifier	Separation ($''$)	Position Angle ($^\circ$)
06295+3414	4.25 ± 0.14	256.8 ± 0.6
06051+3016	11.74 ± 0.40	177.3 ± 0.6
06508+2927	6.60 ± 0.22	23.7 ± 0.6

Note.
[a] All observations were made in the MKO K band on UT 2012 February 25.

precise than, estimates derived from several of our more poorly focused MOIRCS frames.

4.2.2. IRTF/SpeX K-band Lucky Imaging

The well-focused Subaru image described above motivated us to acquire additional images of Bergfors-6. On 2012 February 25 (UT) we imaged the WASP-12 system with the IRTF/SpeX guide camera (Rayner et al. 2003), which uses a 512^2 Aladdin 2 Insb array with a plate scale of $0\farcs1185$ pixel^{-1}. Observing through sometimes patchy clouds, we acquired 1200 0.4 s $K_{\rm MKO}$ (Tokunaga et al. 2002) frames (from airmass 1.2 to 1.5) and 900 0.21 s $J_{\rm MKO}$ frames (from airmass 1.5 to 2.2). In all observations we held the SpeX instrument rotator at a position angle of 90°. The J-band data were not sufficient to reliably detect Bergfors-6 (presumably because of the increased noise penalties resulting from the use of very short exposures and the smaller total integration time); hereafter, we discuss only the K-band data.

We calibrate the SpeX images using a median stack of internal (thermal) flat fields and subsequently perform bilinear interpolation over a few noticeably bad pixels. We select the top 10% of all frames on the basis of the peak pixel flux near the location of WASP-12, then use the "shift and add" algorithm to align and stack these frames (our signal to noise ratio (S/N) is too low for more advanced algorithms; Jefferies & Christou 1993; Schoedel et al. 2011). Changing the fraction of frames used in our analysis from 5% to 40% leaves our results unchanged within our estimated uncertainties. (However, our most selective analyses (which use only 1%–2% of the data) show a hint of north–south elongation $\lesssim 0\farcs3$. Though the resulting image is quite noisy, we note that the initial discovery image (Bergfors et al. 2011, 2012) also shows a similar elongation. We recommend additional high-resolution imaging of Bergfors-6 to test this elongation.) The final image from our standard (10%) analysis is shown in Figure 4: in this image WASP-12 exhibits an axisymmetric PSF with a Strehl ratio of roughly 8% and a FWHM of $0\farcs33$ (roughly a factor of three better than the seeing-limited resolution).

For astrometric reference, we observed three known multiple systems taken from Version 2012-02-12 of the Washington Visual Double Star Catalog (WDS 06295+3414, 06051+3016, and 06508+2927; Mason et al. 2001) moderately near WASP-12, with comparable magnitudes to WASP-12, and with separations of $4''$–$12''$. We took 20 0.5–1 s frames of each system in the same region of the detector as our WASP-12 images, and in each frame we compute the centroids of both components using standard IRAF tasks. From these measurements and their dispersion, we derive a SpeX guider plate scale of $0\farcs116 \pm 0\farcs004$ and an intrinsic field rotation (i.e., true position angle minus measured position angle) of $-0\fdg5 \pm 0\fdg6$. We adopt these values in our subsequent analysis and list our astrometry of the WDS stars in Table 3.

We determine the flux ratio of the two stars using aperture photometry. Bergfors-6 is located in the PSF wings of WASP-12, so we must account for this contamination. Because our PSF is quite symmetric (though distinctly non-Gaussian) we compute an average radial profile for WASP-12 (after masking out the 90° wedge of sky directed toward Bergfors-6). We re-interpolate this one-dimensional profile into a two-dimensional model PSF. We estimate the uncertainty of the profile by taking the standard

deviation on the mean in each annular bin, and propagate these uncertainties along with the combined photon and read noise. We then subtract the WASP-12 model PSF from the image and compute partial-pixel aperture photometry at the locations of Bergfors-6 and WASP-12. Residuals are still apparent near the center of WASP-12, so we restrict our analysis to smaller apertures: an inner aperture radius of 2.5 pixels provides the highest S/N (and least evidence for contamination) for Bergfors-6, so we use this aperture for both systems. Our final estimate of the $K_{\rm MKO}$ flux ratio is listed in Table 2, and is consistent with our narrowband MOIRCS measurement.

We measure the relative astrometry of WASP-12 and Bergfors-6 by computing the centroid of WASP-12 in the speckle image, and of Bergfors-6 in the profile-subtracted image. We estimate the uncertainties in these measurements by bootstrap resampling (Press 2002), in which we repeat our analysis many times using synthetic data sets, constructed by sampling (with replacement) our original set of 1200 images. We list the separation and position angle derived from the IRTF speckle data in Table 2.

4.2.3. Spitzer/IRAC Imaging

We also examined *Spitzer*/IRAC subarray data (3.6 and 4.5 μm, from Cowan et al. 2012) to search for evidence of Bergfors-6. We performed a weighted least-squares fit to each median stack of 64 subarray frames (using the pixel uncertainties provided by the IRAC calibration pipeline, Version 18.18.0) by linearly interpolating the appropriate 5× oversampled point response functions[10] (PRF) to account for subpixel motions.

We do see evidence for an additional point source in the IRAC data, located approximately 1–2 pixels west–southwest of WASP-12. However, we are unable to measure precise astrometry or relative photometry with these data for several reasons. First, the IRAC plate scale ($1\farcs09$ pixel^{-1}) is comparable to the WASP-12/Bergfors-6 separation; second, the IRAC PSF is undersampled at these wavelengths. Consequently, we see clear evidence for oversubtraction in the PRF fitting at the location of Bergfors-6, so we cannot reliably determine the system flux ratio (de-weighting the pixels closest to Bergfors-6, but offset from the WASP-12 core, does not change this result). From these measurements we estimate a flux ratio of $>7\%$ in the two IRAC channels, consistent with our ultimate interpretation of Bergfors-6 as a cool stellar object.

4.2.4. Keck/NIRSPEC Spectroscopy

We searched online data archives for additional evidence of Bergfors-6, and found a set of high-resolution *K*-band spectra taken with Keck/NIRSPEC, a high-resolution, cryogenic, echelle, NIR spectrograph (McLean et al. 1998), on UT 2010 April 22 (Keck Program ID C269NS; PI: G. Blake). This data set consists of 16 four-minute integrations of WASP-12 taken using the $0\farcs432 \times 24''$ slit. The WASP-12 observations were taken at a position angle of $\sim 73^\circ$ (roughly aligned with WASP-12 and Bergfors-6), and the seeing was sufficiently good to distinctly resolve the two components in the spectra.

We extract our spectra using our own set of Python tools to trace the spectra in the dark-corrected and flat-fielded NIRSPEC frames. In each echelle order of each frame, we compute a high S/N mean spectral profile by collapsing the trace along the dispersion direction and fit two Gaussian functions to this profile: this provides an estimate of the projected separation of WASP-12 and Bergfors-6 in each frame. We then fit two Gaussian functions to each resolution element while holding constant the positions of the two sources: the amplitude of each Gaussian represents the flux in that wavelength element. We then compute weighted means from the individual extracted spectra and estimate uncertainties by measuring the variations in each pixel, after excluding points deviating by $>3\sigma$.

Using a high-resolution simulated telluric spectrum (generated using ATRAN; Lord 1992), we identify known telluric lines and compute a best-fit dispersion function in each echelle order. Estimating a line centroid precision of 0.5 pixels, we find that a cubic or quartic polynomial minimizes the BIC of these fits. The residuals to our dispersion solutions have RMS values $\lesssim$0.1 Å and maximum excursions of $<$0.2 Å.

In the raw NIRSPEC frames the spatial axis of the slit is not aligned with the NIRSPEC detector columns, so spectra taken at the A and B nod positions are offset from each other. We spline-interpolate the spectrum in each echelle order and cross-correlate it at subpixel increments with a high S/N template spectrum (Deming et al. 2005). We construct our template by taking the temporal average, after removing outliers, of all our spectra. A parabolic fit to the peak of each spectrum's cross-correlation provides the optimal offset value, and we then spline-interpolate all the spectra to a single, common reference frame. We then combine the resulting set of aligned spectra (excluding outlying points) and thereby provide a set of simultaneous high-resolution spectra of both WASP-12 and Bergfors-6. The spectra of WASP-12 and Bergfors-6 have median S/N values of 203 and 32 pixel^{-1}, respectively.

Because the two spectra are obtained simultaneously and the objects are separated by only $1''$ we expect the telluric signature in both spectra to be indistinguishable. We therefore divide the spectrum of Bergfors-6 by that of WASP-12 to remove the effect of telluric absorption. Possible misalignment of the spectrograph slit prevent these data from usefully constraining the absolute flux ratio of these two objects, but the data constrain tightly Bergfors-6's spectral type from the relative strengths of individual spectral features. The NIRSPEC spectra do not cover the wavelengths of standard gravity indicators such as Na or Ca lines, so our subsequent analysis focuses on the two most prominent gravity-sensitive features covered by these data: the ^{12}CO (2, 0) and (4, 2) band heads located at 2.294 and 2.353 μm (Kleinmann & Hall 1986). As we now describe, we find that Bergfors-6 is a hot M dwarf.

4.3. The Spectral Type and Nature of Bergfors-6

4.3.1. Photometric Constraints

With our four (i, z, $K_{\rm MKO}$, K_{2315}) relative photometric measurements and the NIRSPEC spectrum we determine the spectral type of Bergfors-6, as described below. First, we apply the relationship between spectral type and absolute magnitude of Kraus & Hillenbrand (2007) using our photometry. This relationship is for main-sequence stars, and WASP-12 is 25% larger than a zero-age main-sequence star of the same mass (Hebb et al. 2009; Torres et al. 2010). Accounting for this, and assuming $T_{\rm eff} = 6300 \pm 100$ K, gives a distance modulus for WASP-12 of $\mu_{\rm W12} = 7.7 \pm 0.2$ mag (significantly nearer than the previous estimate; Chan et al. 2011). For Bergfors-6, our estimate of the $i - K$ color (after applying the color transformations of Carpenter 2001) implies a main-sequence spectral type of M0–M1 ($T_{\rm eff} = 3700 \pm 100$ K). Assuming systematic

[10] Available at http://irsa.ipac.caltech.edu/data/SPITZER/docs/irac/calibrationfiles/psfprf/

uncertainties of 0.2 mag gives $\mu_{B6} = 7.1 \pm 0.2$ mag, rather closer than WASP-12 if Bergfors-6 is still on the main sequence. That Bergfors-6 is closer to Earth than is WASP-12 is the opposite of the trend noted by Daemgen et al. (2009), who uniformly estimated that their faint companions to planet host stars were more distant than the brighter component.

Next, we fit only the relative (Bergfors-6/WASP-12) stellar photometry using low-resolution stellar atmosphere models (Castelli & Kurucz 2004). We interpolate to the effective temperature, [Fe/H], and surface gravity of WASP-12 and hold these values fixed in the modeling. For Bergfors-6 we assume a metallicity equal to that of WASP-12 and allow three free parameters: surface gravity, effective temperature, and a geometric factor ($f = (R_{B6}/R_{W12})(d_{W12}/d_{B6})$) relating the relative sizes and heliocentric distances of the two stars. A standard Pythonic minimizer and an MCMC analysis using the `emcee` affine-invariant sampler (Foreman-Mackey et al. 2012) provide the desired physical parameters and their uncertainties. The derived parameters for Bergfors-6 are 3840 ± 70 K (which agrees well with our previous estimate of this object's effective temperature) and $f = 0.452 \pm 0.015$; the covariance between these parameters is -1.73 K.

We also considered that Bergfors-6 might be an extragalactic, rather than a stellar, contaminant (Luhman & Mamajek 2010). However, a comparison of its photometric spectral energy distribution (SED) with low-resolution galactic spectral templates (Assef et al. 2010) suggests that this explanation is unlikely.

4.3.2. Spectroscopic Constraints

Spectroscopy is particularly well suited to constrain surface gravity. We now use both the NIRSPEC spectrum and the relative photometry described above to constrain Bergfors-6's parameters, again using the `emcee` MCMC sampler (Foreman-Mackey et al. 2012). For this analysis, we use the BT-Settl library[11] computed using the `PHOENIX` atmosphere code (Allard et al. 2011). This library provides high-resolution model spectra across a wide range of parameter space. We use the so-called hot models using abundances from Asplund et al. (2009) with no alpha enhancement. As noted previously, we use only the two NIRSPEC echelle orders that cover CO band-head features—the wavelengths from 2.273 to 2.308 μm and 2.344 to 2.380 μm.

For a given set of input parameters, our spectral modeling algorithm begins by logarithmically interpolating between BT-Settl models at the nearest values of $T_{\rm eff}$, $\log g$, and [M/H]. The model then applies (1) a Doppler shift, (2) a quadratic continuum normalization (because the absolute slope and curvature of the spectrum is unknown owing to possible slit misalignments), and (3) a convolution with a Gaussian kernel of specified width. Finally, we bin (not interpolate) the model spectrum onto our NIRSPEC pixel grid and compute relative broadband photometry as described in the preceding section—except that here we propagate the uncertainties in WASP-12's parameters into the modeling by performing a random draw from normal distributions in $T_{\rm eff}$, $\log g$, and [M/H] at each step in the MCMC analysis that follows.

In our analysis the spectral type of Bergfors-6 is constrained almost entirely by the ~2000 spectroscopic data points, while the geometric ratio $(R_{B6}/R_{W12})(d_{W12}/d_{B6})$ is constrained only by the broadband photometry. The results of this analysis for Bergfors-6 are an effective temperature of 3660^{+85}_{-60} K and a $\log g$ (cgs) of $5.13^{+0.38}_{-0.22}$; we show our best-fit model spectrum in Figure 5. Our derived parameters are fully consistent with an M0 dwarf on the main sequence, which would imply a radius of 0.5–0.6 $R_\odot$ (Torres et al. 2010). The geometric ratio from our analysis is $0.520^{+0.027}_{-0.037}$, which implies a radius 50% larger than expected for a main-sequence dwarf lying at the same distance at WASP-12. Our spectral analysis therefore suggests that Bergfors-6 lies approximately 50% closer to Earth than does WASP-12 and that it represents a chance foreground alignment.

[11] Available online at http://phoenix.ens-lyon.fr/

4.4. Radial Velocities

To estimate the radial velocities of the two stellar components in our telluric-corrected Bergfors-6/WASP-12 ratio spectrum we cross-correlate with BT-Settl models (Allard et al. 2011). We cross-correlate each echelle order of the ratio spectrum with models with effective temperatures of 6200 and 3800 K. We also cross-correlate the spectra (before telluric correction) with the high-resolution atmospheric transmission profile of Hinkle et al. (2003) to establish our observational reference frame.

The radial velocity of Bergfors-6 is constrained mainly by the strong CO bands lying redward of 2.29 μm, while WASP-12's is tightly constrained only by the broad (FWHM = 8.1 Å) Brackett γ line. After correcting for the Earth's velocity along the line of sight (using the Python routine `astrolib.baryvel`), we estimate radial velocities for WASP-12 and Bergfors-6 of 16.5 ± 2.6 and 19.7 ± 1.3 km s^{-1}, respectively. These values are consistent with the radial velocity of 19.1 km s^{-1} derived from WASP-12b's initial radial velocity measurements (Hebb et al. 2009; Campo et al. 2011). This common velocity is consistent with a scenario in which either WASP-12 and Bergfors-6 are gravitationally bound and share a common three-dimensional space motion, or in which the consistency of the two stars' radial velocities is merely a coincidence.

We also find no evidence for multiple spectral line profiles, which would indicate that Bergfors-6 is an unresolved binary. The cross-correlation profiles of our data and spectral template have FWHMs of approximately 14 km s^{-1}. All three echelle orders containing strong CO features (centered on 2.29, 2.36, and 2.44 μm) show unimodal cross-correlation peaks and no evidence of the secondary peaks that would suggest an additional cool companion. Thus Bergfors-6 shows no spectroscopic evidence of binarity.

4.5. Interpretation of Bergfors-6

We conclude that Bergfors-6 is a cool star showing absorption features consistent with a high surface gravity. Our spectroscopy implies that Bergfors-6 is a main-sequence star, and our relative photometry suggests that Bergfors-6 lies 50% closer to Earth than does WASP-12. In this scenario, the hint of elongation alluded to in Section 4.2.2 is spurious and the consistent radial velocities of WASP-12 and Bergfors-6 is coincidental. However, if Bergfors-6 were a binary M dwarf system observed near conjunction, then the binary and WASP-12 could lie at the same distance from Earth; if the three components were bound this scenario would offer a natural explanation for the consistent systemic velocities. Because of the intriguing possibilities inherent in a gravitationally bound arrangement, we briefly discuss the implications of such a scenario below.

At the distance of WASP-12, the projected separation of Bergfors-6 is roughly 400 ± 100 AU. Such an object would have an orbital period of several thousand years, and as such would be marginally compatible with the inferred upper limit of binary separation (~300 AU) needed to substantially influence

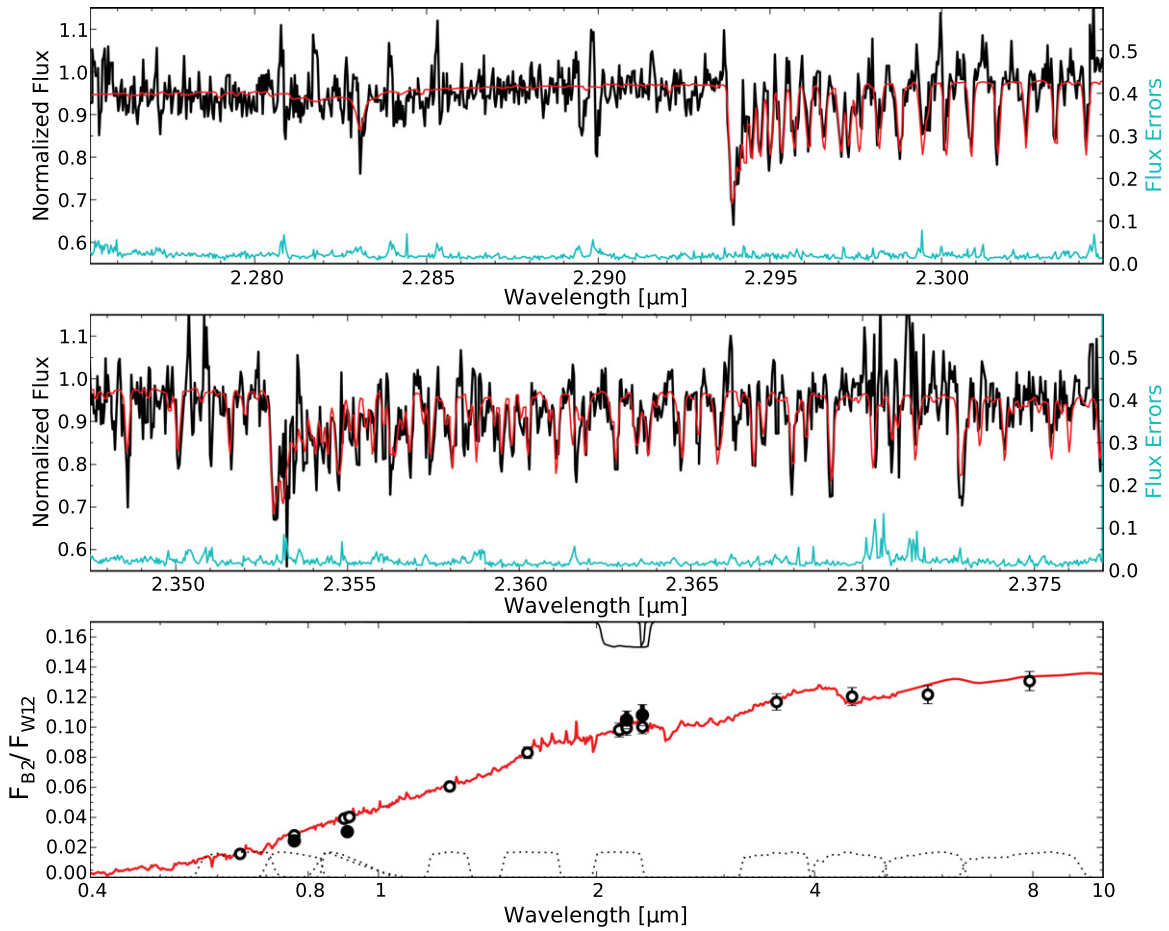

Figure 5. Keck/NIRSPEC spectrum of Bergfors-6 (black curve, top and middle) and relative photometry of WASP-12 and Bergfors-6 (filled points, bottom), and our best-fit Phoenix/BT-Settl model (red curve). As discussed in Section 4.3, the ensemble of measurements suggests that Bergfors-6 is a hot M dwarf located 50% closer to Earth than WASP-12. Top and middle: the blue curves show our estimated spectroscopic measurement uncertainties; the vertical scale for these curves is indicated at right. Bottom: the open points at bottom are the inferred photometric dilutions of transits or occultations measured in various bandpasses (tabulated in Table 4); we indicate filters used in this analysis with solid lines, while other filters are denoted with dashed lines. The error bars of the open points represent the 68.3% confidence intervals on these dilution estimates, taking into account the uncertainties in our fit.

(A color version of this figure is available in the online journal.)

planetary migration and dynamics (Desidera & Barbieri 2007). Assuming that Bergfors-6 is near apastron implies a Kozai oscillation timescale (Fabrycky & Tremaine 2007) of (very roughly) $20[(1-e_{B6})/(1+e_{B6})]^{3/2}$ Gyr, where e_{B6} is Bergfors-6's orbital eccentricity. For substantial Kozai interactions to have taken place during WASP-12's lifetime (Hebb et al. 2009; Chan et al. 2011), we thus require $e_{B6} > 0.7$. Long-period binaries with such high eccentricities are rare, but they do exist (Duquennoy & Mayor 1991).

Fabrycky & Tremaine (2007) predict that hot Jupiter systems with an additional, widely separated stellar component will preferentially exhibit misalignment between their stellar spin and planetary orbital axes. Recent observations of WASP-12 have determined that the sky-projected angle between the spin and orbital axes is 59^{+20}_{-15} deg, strongly suggesting a misaligned system (Albrecht et al. 2012). This may be circumstantial evidence that WASP-12 has migrated via Kozai interactions and that a long-period bound companion is required (e.g., Ibgui et al. 2011).

Ultimately, high-resolution imaging can most quickly determine whether WASP-12 and Bergfors-6 truly exhibit common proper motion and are gravitationally bound, and whether Bergfors-6 is a single or multiple system. Based on WASP-12's proper motion (~8 mas yr^{-1}; Zacharias et al. 2004), speckle or seeing-limited astrometry of the type presented here will not be sufficient for this purpose. However, a two-year baseline of large-aperture adaptive optics imaging (Yelda et al. 2010) could suffice to confirm or rule out common proper motion.

5. REVISING PAST TRANSIT AND SECONDARY ECLIPSES

Because Bergfors-6 was not noted in previous transit and secondary eclipse observations of WASP-12b, these flux diminutions were diluted by this faint star's constant baseline flux. This effect is largest in the infrared; the results of optical observations change by only a few percent, less than their typical uncertainties. Although a full re-evaluation of WASP-12's system parameters is beyond the scope of this work, we correct the depth measurements for the contamination effect and present revised transit and occultation depths below. We propagate the uncertainties in Bergfors-6's effective temperature into our estimates of the photometric dilution caused by Bergfors-6, which we list in Table 4. In some secondary eclipses, and in all transits, the corrections we apply change the previously reported depths by $>1\sigma$.

Table 4
Dilution Factors and Corrected WASP-12b Transit and Occultation Depths

Filter	Reported Depth	Aperture Fraction	Dilution Fraction	Corrected Depth	Reference[a]
z	0.00082 ± 0.00015	1.000 ± 0.000	0.0397 ± 0.0017	0.00085 ± 0.00016	LM10
J	0.00131 ± 0.00028	1.000 ± 0.000	0.0606 ± 0.0029	0.00139 ± 0.00030	Cr11
H	0.00176 ± 0.00018	1.000 ± 0.000	0.0830 ± 0.0039	0.00191 ± 0.00020	Cr11
Ks	0.00309 ± 0.00013	1.000 ± 0.000	0.0981 ± 0.0047	0.00339 ± 0.00014	Cr11
Ks (MKO)	0.00281 ± 0.00085	1.000 ± 0.000	0.0994 ± 0.0047	0.00309 ± 0.00093	Z12
NB2315	0.0041 ± 0.0005	1.000 ± 0.000	0.1002 ± 0.0045	0.0045 ± 0.0006	This work
IRAC CH1	0.00379 ± 0.00013	0.902 ± 0.018	0.1168 ± 0.0055	0.00419 ± 0.00014	Ca11
IRAC CH2	0.00382 ± 0.00019	0.911 ± 0.016	0.1204 ± 0.0060	0.00424 ± 0.00021	Ca11
IRAC CH3	0.00629 ± 0.00052	0.855 ± 0.036	0.1217 ± 0.0060	0.00694 ± 0.00057	Ca11
IRAC CH4	0.00636 ± 0.00067	0.788 ± 0.068	0.1307 ± 0.0063	0.00701 ± 0.00074	Ca11
IRAC CH1	0.0033 ± 0.0004	0.850 ± 0.038	0.1168 ± 0.0055	0.00363 ± 0.00044	Co12
IRAC CH2	0.0039 ± 0.0003	0.833 ± 0.049	0.1204 ± 0.0060	0.00429 ± 0.00033	Co12
IRAC CH2	0.0050 ± 0.0004	0.833 ± 0.049	0.1204 ± 0.0060	0.00550 ± 0.00044	Co12 (null)[b]
V/i'[c]	0.01252 ± 0.00045	0.230 ± 0.100	0.0186 ± 0.0023	0.01257 ± 0.00045	C11[c]
IRAC CH2	0.0126 ± 0.0004	0.833 ± 0.049	0.1204 ± 0.0060	0.01386 ± 0.00044	Co12 (null)[b]
IRAC CH1	0.0125 ± 0.0003	0.850 ± 0.038	0.1168 ± 0.0055	0.01374 ± 0.00033	Co12
IRAC CH2	0.0112 ± 0.0004	0.833 ± 0.049	0.1204 ± 0.0060	0.01232 ± 0.00044	Co12
Johnson R	0.01380 ± 0.00016	1.000 ± 0.000	0.01571 ± 0.00096	0.01402 ± 0.00016	M11
B	...	...	0.0045 ± 0.0015	...	...
V	...	...	0.0090 ± 0.0030	...	...
i'	...	...	0.0281 ± 0.0014	...	...

Notes.
[a] (LM10) López-Morales et al. 2010; (Cr11) Croll et al. 2011; (Z12) Zhao et al. 2012; (Ca11) Campo et al. 2011; (Co12) Cowan et al. 2012; (M11) Maciejewski et al. 2011; (C11) Chan et al. 2011.
[b] Results from the "null hypothesis" of Cowan et al. (2012), which assumes zero ellipsoidal variation in their 4.5 μm observations.
[c] These transit analyses average multiple photometric bands, so their correction factors may be less precise. See Section 5.

Essentially all the light from Bergfors-6 lies within the apertures of ground-based observations (Hebb et al. 2009; López-Morales et al. 2010; Croll et al. 2011; Chan et al. 2011; Maciejewski et al. 2011; Zhao et al. 2012), but *Spitzer*/IRAC analyses use narrower apertures (Campo et al. 2011; Cowan et al. 2012) and so only a portion of Bergfors-6's starlight contaminates these secondary eclipse measurement. To estimate the IRAC contamination fraction we generate 10× super-sampled PSFs for all four IRAC channels,[12] using a 6300 K blackbody spectrum simulated at the center of the instrument field of view. We then compute aperture photometry using the reported photometric aperture diameters (Campo et al. 2011; Cowan et al. 2012) at a position offset by 1.″05 from the PSF center to estimate how much of Bergfors-6's flux fell into the WASP-12 aperture in these analyses. We ignore possible time-variable illumination caused by the intrapixel effect (Charbonneau et al. 2005). Note that the phase curve observations of Cowan et al. (2012) are also diluted by Bergfors-6, and must be revised upward by the same factors as indicated in Table 4. This in turn increases the ellipsoidal variation inferred from these measurements, placing the IRAC 4.5 μm results in even stronger conflict with those from WFC3 (Swain et al. 2012).

The correction of optical transit measurements is complicated by the common, but deplorable, practice of reporting a single transit depth when using observations taken in different bandpasses (Hebb et al. 2009; Chan et al. 2011). Atmospheric characterization via transit observations depends on the fundamentally wavelength-dependent planetary radius during transit, and so we recommend that future analyses of multiple photometric data sets report the transit depths measured in each bandpass in addition to a single, achromatic value. In addition, such analyses are not always clear about the relative weighting of data points from separate observations. Nonetheless, we attempt to estimate the relative weightings and derive appropriate correction factors for prior multi-band optical transit observations of WASP-12.

The analysis of Maciejewski et al. (2011) used only a single bandpass (Johnson R) and so their Johnson R transit depth is the most reliable optical transit measurement in Table 4. The analysis of Chan et al. (2011) uses two transit data sets: 671 V-band and 470 i'-band observations with residual RMS values of 2.0 and 1.2 mmag, respectively. This work uses an additional multiplicative term to increase the per-point data uncertainties (1.48 and 1.57, respectively). Assuming that the statistics of the final reported transit depth behaves similarly to a weighted mean, we estimate that the two data sets constrain the transit parameters with roughly equal weight.

We use these weights to determine a weighted average of the correction factors for each bandpass. Such a weighted average is only a rough approximation to the true correction factor, so the correction factors for these analyses are somewhat less certain. We thank the referee for pointing out that the situation is even more muddled for the discovery paper (Hebb et al. 2009), which uses three transit data sets: 227 B band, 614 z' band, and 6393 SuperWASP (roughly V band) observations. Because Hebb et al. (2009) do not report the residual RMS scatter of the SuperWASP photometry, we do not attempt to determine the relative weighting of these several transit observations and we do not report a mean dilution-corrected transit depth for these data.

The dilution correction factors, and dilution-corrected transit and occultation depths, are listed in Table 4. The optical transit

[12] Using Tiny Tim; available at http://ssc.spitzer.caltech.edu/

depths in particular are increased by a few percent, and the planetary radius increases by only half this factor. Owing to current uncertainties in stellar properties, such an effect is smaller than current uncertainties on WASP-12b's physical radius.

6. EMISSION SPECTRUM AND ATMOSPHERIC PROPERTIES

We now return out attention to the nature of WASP-12b's atmosphere as constrained by its SED. In our narrow bandpass we find a brightness temperature of 3640 ± 230 K by using the model stellar spectrum described in the following section, modeling WASP-12b's emission in our bandpass as a blackbody, and propagating the 1σ uncertainties in our occultation measurement. This brightness temperature is rather higher than the planet's equilibrium temperature of 2990 ± 110 K (computed using the Bond albedo and recirculation efficiencies from Cowan et al. 2012) and is higher than inferred in any broad photometric bandpass (López-Morales et al. 2010; Croll et al. 2011; Campo et al. 2011; Cowan et al. 2012). The Canada–France–Hawaii Telescope/WIRCam Ks filter cuts off just where the NB2315 filter cuts in, so our measurement is not in conflict with this previous secondary eclipse observation (Croll et al. 2011).

In the following, we use the weighted averages of the two sets of IRAC (3.6 and 4.5 μm) measurements (Campo et al. 2011; Cowan et al. 2012; see also Table 4). Two possible 4.5 μm secondary eclipse depths were reported by Cowan et al. (2012), and we use their "null hypothesis" consistent with no ellipsoidal variations (as implied by the constraints placed on WASP-12b's shape by Swain et al. 2012).

We first introduce the improved, model-independent constraints these observations place on WASP-12b's bolometric luminosity in Section 6.1, and then discuss our efforts to generate a coherent model of the planet's emission spectrum in Section 6.2.

6.1. Bolometric Luminosity

WASP-12b has one of the best-determined bolometric luminosities of any extrasolar planet (Cowan & Agol 2011). In an earlier work (Crossfield et al. 2012), we discussed the current constraints on the bolometric luminosity of WASP-12b. Here we update this analysis in light of our dilution-corrected occultation measurements and recent *Spitzer*/IRAC and *HST*/WFC3 observations (Cowan et al. 2012; Swain et al. 2012).

Current measurements now constrain the planet's dayside to have $L_{\rm bol} = (3.6\text{–}5.0) \times 10^{30}$ erg s^{-1}, where the lower limit assumes the case of zero emission between the observed bandpasses. Here we have followed the same approach as our previous calculation, but we now use the WFC3 spectrum (Swain et al. 2012) from 1.1 to 1.485 μm (replacing the J-band eclipse, but retaining the H-band eclipse, of Croll et al. 2011). In this analysis our narrowband measurement, and the controversy over the IRAC 4.5 μm measurement, affect the luminosity by only 0.1×10^{30} erg s^{-1}.

On the basis of thermal occultation and phase curve measurements, WASP-12b's bolometric albedo has been inferred to be $A_B = 0.25 \pm 0.1$ (Cowan et al. 2012), which implies that the planet absorbs $(3.8 \pm 0.8) \times 10^{30}$ erg s^{-1} from its host star. Following the approach of Crossfield et al. (2012), we find that this value constrains the nightside luminosity to be $<1.6 \times 10^{30}$ erg s^{-1}, consistent with the nightside luminosity inferred by Cowan et al. (2012) of $0.06^{+0.12}_{-0.02} \times 10^{30}$ erg s^{-1}. This last point further assumes that the nightside (like the dayside; see below) emits approximately like a blackbody.

We are thus nearing a bolometric luminosity sufficiently well constrained that we can test evolutionary models of this planet. The current uncertainty in $L_{\rm bol}$ is dominated by measurements at the shortest wavelengths, suggesting that occultation observations at wavelengths <1 μm may be the best next step toward an even more tightly constrained bolometric luminosity.

6.2. Atmospheric Models

The first systematic effort to retrieve WASP-12b's atmospheric parameters (using infrared broadband secondary eclipse photometry) inferred a high C/O (>1) and ruled out any strong temperature inversion at the pressures probed (0.01–2 bar; Madhusudhan et al. 2011). That study published several representative models, all of which had $\chi^2 \sim 10$ with seven measurements and $\sim$10 free parameters (BIC $\sim$ 32). These models also predicted a strong absorption feature (depth $\lesssim$ 0.2%) at 2.315 μm: our narrowband secondary eclipse measurement rules out this absorption feature at $>3\sigma$. This narrowband result, our characterization of Bergfors-6 and correction for its diluting effect, and the alternative *Spitzer*/IRAC 4.5 μm eclipse depth of Cowan et al. (2012) all indicate the need for a new analysis of WASP-12b's atmospheric properties.

To better understand the nature of the planet's dayside emission we constructed a variety of atmosphere models for WASP-12b, following Barman et al. (2001, 2005). We compared model SEDs to the corrected occultation depths from Table 4. For this exercise we adopt the Cowan et al. (2012) 4.5 μm value without ellipsoidal variations (their "null hypothesis"). As discussed by Cowan et al., when ellipsoidal variations are allowed, the inferred planet elongation in this band is substantially larger than expected. Indeed, recent NIR *HST*/WFC3 observations exclude the large ellipsoidal variations inferred from the *Spitzer*/IRAC analysis (Swain et al. 2012). Furthermore, the measured primary transit radius at 4.5 μm differs dramatically from radii at other wavelengths as well as predicted transit spectra. Given that two very unexpected physical properties are required to explain the ellipsoidal variations, the 4.5 μm secondary eclipse value without ellipsoidal variations is likely more reliable (N. B. Cowan 2012, private communication). Finally, our ultimate result—that the high C/O result is not justified by current photometric data—does not change even if we use the average of the Campo et al. and Cowan et al. results.

By far the model that best matches the broadband occultation photometry is a 3000 K blackbody (see the upper panel of Figure 6, and Figure 7), with $\chi^2 = 15$ with only two free parameters (BIC = 19). Taking the mean of the Campo et al. and Cowan et al. results gives a blackbody model with higher $\chi^2 = 25$ and BIC = 29, but this BIC value is still smaller than that for the high C/O models as discussed above. This lower BIC value indicates that current observations do not justify the use of these more complicated models. Our best-fit blackbody temperature matches the expected equilibrium temperature of the planet if redistribution of heat to the nightside is extremely inefficient. The close match to a blackbody also indicates that the planet's photosphere is nearly isothermal at the depths probed by these wavelengths.

Our default irradiated atmosphere model assumes zero redistribution of heat to the nightside (consistent with the blackbody analysis) and metal abundances matching those of the host star ([Fe/H] = 0.3). This model predicts a temperature inversion

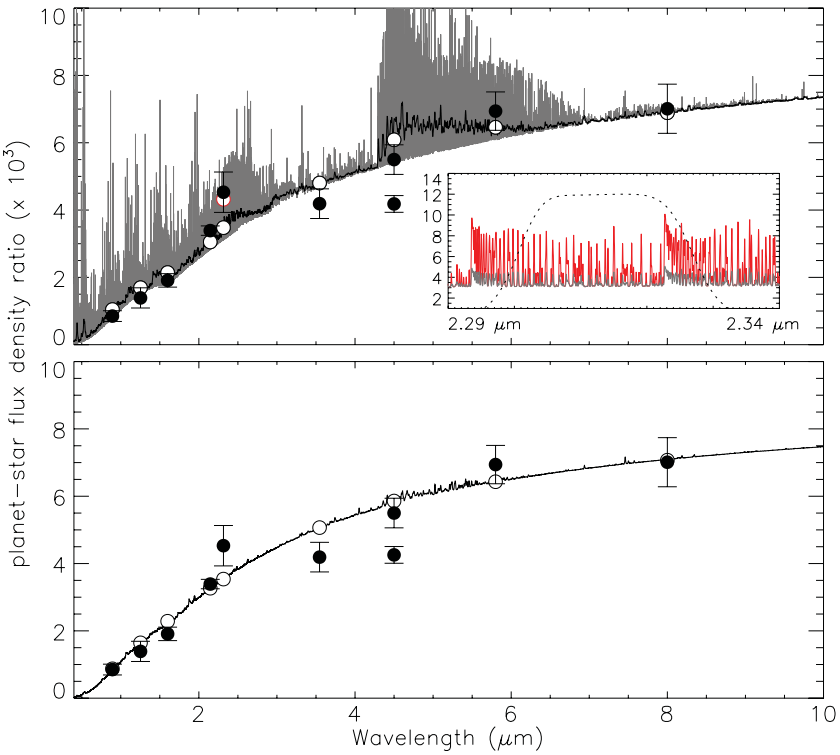

Figure 6. WASP-12b emission spectrum; see Section 6 for a full discussion. Solid points are the dilution-corrected photometric secondary eclipse depths listed in Table 4; at 4.5 μm we plot the results of both Campo et al. (2011) and Cowan et al. (2012). The lower panel is the blackbody comparison (open symbols are the model, band-integrated, points). The upper panel includes several spectra: the dark black spectrum (with open black symbols) is our solar abundance, 2π redistribution model spectrum (smoothed for plotting purposes by convolving with a Gaussian of FWHM = 100 Å). The gray spectrum reproduces the black model but is plotted at 100 times higher resolution to show the many narrow emission lines predicted by this model. The inset shows the narrowband region and a model with CO lines scaled up (red curve). Within the inset plot, the "standard" high-res model is also shown in the same gray color as in the main figure. Note the scale: these lines are narrow but very bright. If such strong, narrow emission lines are present, they should be easily discerned by future observations.

(A color version of this figure is available in the online journal.)

above an isothermal region (Figure 7); it also has $\chi^2 = 15$; since it has substantially more free parameters than a blackbody, the BIC for this model fit is substantially worse than for the simpler model in the previous paragraph. In such a model, the inversion extends partially across the IR photosphere resulting in modestly inverted CO and H_2O bands (see the lower panel of Figure 6). However, the model band-integrated fluxes are similar to the blackbody and match the broadband observations equally well (Figure 6). Naturally, then, the blackbody model provides a substantially lower BIC than the radiative-transfer models (both our model and the models presented by Madhusudhan et al. 2011).

Although our narrowband measurement is fit by the simple blackbody model (within 2σ), we additionally investigated what mechanisms might cause such a narrow band to exhibit a substantially higher flux. In an attempt to reproduce the narrowband flux, we made a number of ad hoc modifications to the temperature–pressure (T–P) profile of the default atmosphere model. The base of the inversion was moved to higher and lower pressures, the steepness of the inversion was altered and several Gaussian temperature perturbations were added. None of these models could match the narrowband flux without negatively impacting the comparison at other wavelengths. A dozen different carbon and oxygen abundances (ranging from 7.7 to 9.4 on the standard base-10 logarithmic scale, where H_2 abundance is exactly 12; these abundances overlap the best-fitting regions from Madhusudhan et al. 2011) were also explored, under the assumption of chemical equilibrium, with similarly negative results. Finally, we constructed a dayside model by dividing the planet's hemisphere into 10 concentric regions centered on the substellar point. These regions were modeled separately, each receiving flux along the line of sight to the star. The outgoing intensities during secondary eclipse, along the line of sight to the observer, were integrated to produce a dayside spectrum following Barman et al. (2005). The predicted limb-to-substellar temperature structure implies a horizontal as well as vertical temperature inversion (i.e., along a path from the substellar point to the terminator at a constant radius or pressure the temperature decreases, then increases again), but the surface-integrated fluxes from this model did not significantly differ from the default one-dimensional model. Our main conclusion from this modeling exercise is that it is very unlikely that strong narrowband emission could be reproduced by a modification to the thermal profile alone, given the strong constraints placed on the SED by the broadband photometry.

As discussed above, the default, one-dimensional, model predicts a steep temperature inversion. A direct consequence of this inversion is a swath of narrow emission lines that form in the inverted atmospheric layers (gray-shaded spectrum in Figure 6). While the narrowband filter does not encompass the complete CO band, it does cover many of the predicted narrow emission lines including the strong 3–1 band. In the default model, these lines are very bright relative to the continuum but are too narrow to significantly impact the photometry. The model exercise above weakens the case for flux increases in the pseudocontinuum, leaving the lines as a potential explanation for the deep narrowband secondary eclipse. If the line fluxes are increased by a factor of two to four, the narrowband photometry

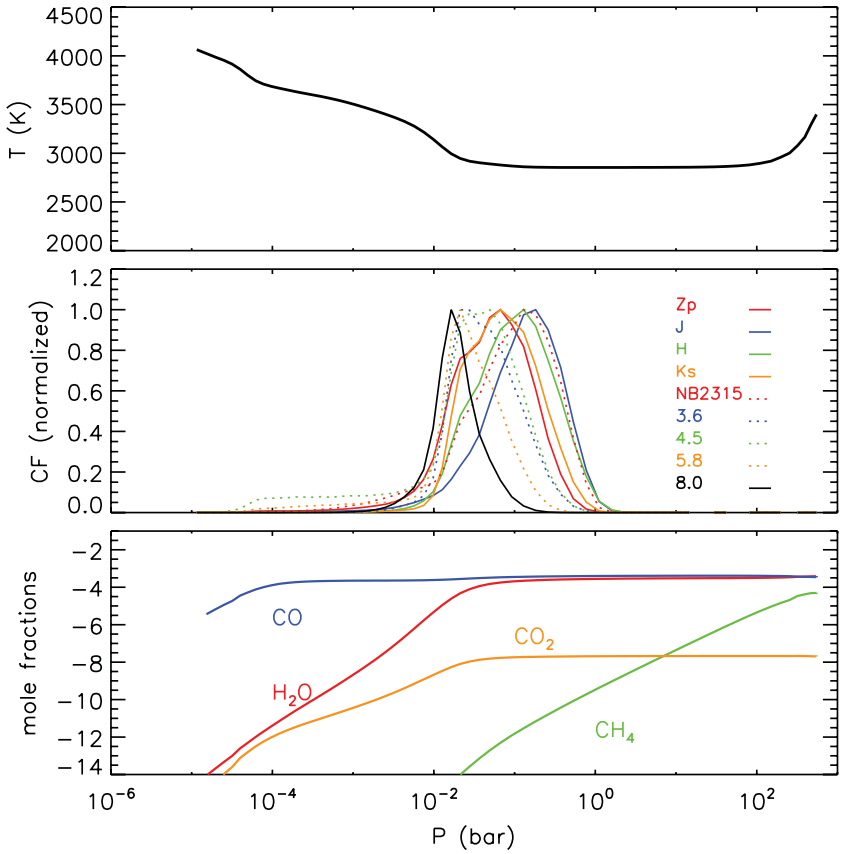

Figure 7. Temperature–pressure profile (top) and molecular abundances (bottom) used to construct the model emission spectrum of WASP-12b shown in Figure 6. The middle panel shows the normalized contribution functions for the indicated filters.

(A color version of this figure is available in the online journal.)

can be reproduced. In this ad hoc scenario, the lines would be extremely bright compared to those of the default model (see comparison in the inset of Figure 6). In the default atmosphere model, CO is the fourth most abundant molecule throughout most of the atmosphere including much the inversion region, as shown in Figure 7. Previous studies have shown that local thermodynamic equilibrium (LTE) is achieved for CO in the atmospheres of isolated late-type stars (Ayres & Wiedemann 1989; Schweitzer et al. 2000), meaning that the CO lines should map the gas temperature. However, Barman et al. (2002) concluded that Na was well out of LTE in the upper atmosphere of the modestly irradiated planet HD 209458b, resulting in strong emission cores for the Na D line profiles. Nevertheless, the LTE assumption has not been tested for molecules in highly irradiated atmospheres. If such strong, narrow emission lines were present in the atmosphere of a hot Jupiter, they should be easily discerned by future observations. Note that while CH_4 also has a strong band head at this wavelength (as observed in the telluric transmission spectrum and in spectra of L dwarfs; cf. Hinkle et al. 2003; Cushing et al. 2005), at the high temperature of WASP-12b atmospheric conditions would have to be much farther from equilibrium for significant CH_4 opacity to be apparent. However, a careful non-LTE study is beyond the scope of this paper and further observational confirmation of the narrowband emission is needed.

The claim of strong, non-LTE CH_4 emission in HD 189733b (Swain et al. 2010), which was based on single-slit IRTF/SpeX spectroscopy, was disputed on the basis of contamination by telluric effects (Mandell et al. 2011). However, the types of spectroscopic contamination discussed by Mandell et al. (2011) do not apply to our narrowband relative photometry. Changes in telluric absorption are a common mode over our narrow field of view and should be removed when we divide the flux from WASP-12 by the comparison star flux. Variable telluric emission should be removed by the combination of global sky frame subtraction and local background subtraction in the aperture photometry process (Section 2.2). As discussed in Section 2.3, though the telluric absorption feature intersecting our narrowband filter could explain the systematic photometric ramp (seen shortly after WASP-12 crosses the meridian; Figure 2 and Section 2.3), it seems unlikely that telluric variations could strongly corrupt the secondary eclipse depth while maintaining such a consistent eclipse duration and time of center (Section 3.3).

Our analysis of the observations to date support a planet with little to no redistribution of flux to the nightside, consistent with Cowan et al. (2012). We also find that photometric observations are well reproduced by a blackbody and are not yet sufficiently precise to justify the use of more complicated models. If WASP-12b has a near-isothermal photosphere, then secondary eclipse data will be poorly suited to reveal significant compositional information. Other highly irradiated giant planets have also been observed to host nearly isothermal infrared photosphere, including the similarly hot WASP-18b (Nymeyer et al. 2011) and perhaps the cooler TrES-2b and TrES-3b (O'Donovan et al. 2009; Croll et al. 2010; Cowan & Agol 2011). If WASP-12b does indeed largely radiate like a blackbody, previous conclusions about composition and the presence or absence of a temperature inversion are significantly weakened. If our narrowband flux measurement is confirmed at higher precision and

this flux is produced by emission lines, there may be hope for high-resolution spectroscopic studies to infer the planet's atmospheric composition and thermal profile (e.g., Barnes et al. 2007; Mandell et al. 2011; Rodler et al. 2012; Brogi et al. 2012).

7. CONCLUSIONS

We have presented a deeper-than-expected secondary eclipse ($0.45\% \pm 0.06\%$) of the very hot Jupiter WASP-12b in a narrow band centered at 2.315 μm. The planet's brightness temperature at this wavelength is 3640 ± 230 K, only marginally consistent with WASP-12b's equilibrium temperature of 2990 ± 110 K (Cowan et al. 2012). Our precision is lower than expected because of an unanticipated systematic trend affecting both sky background and stellar photometry, but we are able to exclude data affected by this trend. The duration and timing of the eclipse we measure from these data are consistent with a circular orbit and with previous measurements (Hebb et al. 2009; Croll et al. 2011; Campo et al. 2011; Cowan et al. 2012).

Using NIR photometry and high-resolution spectroscopy, we find that Bergfors-6, a previously identified object only 1″ from WASP-12 (Bergfors et al. 2011, 2012), is an M dwarf star with $T_{\rm eff} = 3660^{+85}_{-60}$ K. If this object is an unresolved binary with two components of equal mass it could lie at the same distance from Earth as does WASP-12. However, Keck/NIRSPEC spectroscopy shows no evidence for binarity. If single, it likely lies closer to Earth than does WASP-12. Adaptive optics imaging on large-aperture telescopes will be necessary to conduct the proper motion studies necessary to discriminate between these two scenarios. If WASP-12 and Bergfors-6 are gravitationally bound, further simulations (e.g., Ibgui et al. 2011) should be undertaken to determine whether Kozai interactions with an object with Bergfors-6's characteristics could have caused WASP-12b's inward migration and, through tidal pumping, have inflated the planet's radius (Bodenheimer et al. 2001).

Bergfors-6 has heretofore passed unnoticed in previous transit and occultation analyses, which has caused the measured depths of these past events to be underestimated. We use our constraints on Bergfors-6 to infer and correct for the dilution of these past observations, in several cases increasing depths by $>1\sigma$. Thus WASP-12b is rather hotter and slightly larger (by 1%–2%) than previously reported. These changes emphasize the importance of high-resolution imaging surveys in the vicinity of newly discovered transiting planets.

The ensemble of dilution-corrected secondary eclipse measurements suggests that WASP-12b's atmosphere is largely isothermal across the pressures probed by eclipse observations (Figures 6 and 7), with a photospheric temperature of roughly 3000 K. This result implies that previous claims of a high C/O for this planet (Madhusudhan et al. 2011) are not yet justified by the current photometric data. Further observations of the planet's 4.5 μm secondary eclipse depth is certainly warranted to resolve the discrepancy between previous results at this wavelength (Campo et al. 2011; Cowan et al. 2012), as our modeling efforts indicate that achieving such a dramatically lower temperature in the 4.5 μm channel would require a major unexpected change in the opacity source(s) across this bandpass. Regardless, our narrowband measurement alone excludes the models used to infer this high C/O at $>3\sigma$. The lack of absorption at a wavelength where CO, a dominant species in any atmospheric model, should exhibit strong absorption is further evidence for a near-isothermal photosphere. Thus secondary eclipse observations are ill suited to determine WASP-12b's atmospheric composition, and ultimately transmission spectroscopy may be a more successful approach in pursuit of this goal.

WASP-12b is clearly an unusual object, and further observations are clearly warranted. Aside from the need for additional IRAC 4.5 μm occultation photometry as described above, any or all of narrowband photometry (from the ground or, if available, using *HST*/NICMOS), single- or multi-object spectroscopy (Swain et al. 2010; Bean et al. 2010; Mandell et al. 2011; Berta et al. 2012), or perhaps by high-resolution phase curve spectroscopy (Barnes et al. 2007; Brogi et al. 2012; Rodler et al. 2012) could be of great utility. Finally, a better measurement of the planet's three-dimensional shape is also highly desirable, especially given the apparent disagreement between the degree of prolateness inferred by Cowan et al. (2012) and Swain et al. (2012). If WASP-12b is substantially prolate, three-dimensional models, ideally coupled with a general circulation model of the planet's atmospheric dynamics, may also provide important clues toward unraveling the mystery of WASP-12b's atmospheric structure and composition.

We thank N. Cowan for many fruitful discussions about the WASP-12 system, M. Swain and J. Bean for discussions about the systematic trend apparent in our relative photometry, K. Stevenson and J. Harrington for reiterating to us the importance of partial pixels in high-precision aperture photometry, C. Bergfors for discussions of the object she discovered, and our anonymous referee for detailed comments and suggestions which improved the quality of this paper.

I.C. was supported by the UCLA Dissertation Year Fellowship and by EACM. B.H. is supported by NASA through awards issued by JPL/Caltech and the Space Telescope Science Center. T.K. acknowledges the financial support by a Grant-in-Aid for the Scientific Research (No. 21340045) by the Japanese Ministry of Education, Culture, Sports, Science and Technology, with which the NB2315 filter was made. This research has made use of the Exoplanet Orbit Database at http://www.exoplanets.org, the Extrasolar Planet Encyclopedia Explorer at http://www.exoplanet.eu, and free and open-source software provided by the Python, SciPy, and Matplotlib communities. We will gladly distribute our raw data products, or many of our algorithms, to interested parties upon request.

Facilities: Subaru (MOIRCS), IRTF (SPeX), Keck:I, Spitzer (IRAC)

REFERENCES

Albrecht, S., Winn, J. N., Johnson, J. A., et al. 2012, ApJ, 757, 18
Allard, F., Homeier, D., & Freytag, B. 2011, in ASP Conf. Ser. 448, Cool Stars, Stellar Systems, and the Sun, ed. C. M. Johns-Krull, M. K. Browning, & A. A. West (San Francisco, CA: ASP), 91
Asplund, M., Grevesse, N., Sauval, A. J., & Scott, P. 2009, ARA&A, 47, 481
Assef, R. J., Kochanek, C. S., Brodwin, M., et al. 2010, ApJ, 713, 970
Ayres, T. R., & Wiedemann, G. R. 1989, ApJ, 338, 1033
Barman, T. S., Hauschildt, P. H., & Allard, F. 2001, ApJ, 556, 885
Barman, T. S., Hauschildt, P. H., & Allard, F. 2005, ApJ, 632, 1132
Barman, T. S., Hauschildt, P. H., Schweitzer, A., et al. 2002, ApJ, 569, L51
Barnes, J. R., Leigh, C. J., Jones, H. R. A., et al. 2007, MNRAS, 379, 1097
Bean, J. L., Miller-Ricci Kempton, E., & Homeier, D. 2010, Nature, 468, 669
Bergfors, C., Brandner, W., Daemgen, S., et al. 2012, MNRAS, in press (arXiv:1209.4087)
Bergfors, C., Brandner, W., Henning, T., & Daemgen, S. 2011, in IAU Symp. 276, ed. A. Sozzetti, M. G. Lattanzi, & A. P. Boss (Cambridge: Cambridge Univ. Press), 397
Berta, Z. K., Charbonneau, D., Désert, J.-M., et al. 2012, ApJ, 747, 35
Bodenheimer, P., Lin, D. N. C., & Mardling, R. A. 2001, ApJ, 548, 466
Bramich, D. M. 2008, MNRAS, 386, L77
Brogi, M., Snellen, I. A. G., de Kok, R. J., et al. 2012, Nature, 486, 502

Campo, C. J., Harrington, J., Hardy, R. A., et al. 2011, ApJ, 727, 125
Carpenter, J. M. 2001, AJ, 121, 2851
Castelli, F., & Kurucz, R. L. 2004, arXiv:astro-ph/0405087
Chan, T., Ingemyr, M., Winn, J. N., et al. 2011, AJ, 141, 179
Charbonneau, D., Allen, L. E., Megeath, S. T., et al. 2005, ApJ, 626, 523
Cowan, N. B., & Agol, E. 2011, ApJ, 729, 54
Cowan, N. B., Machalek, P., Croll, B., et al. 2012, ApJ, 747, 82
Croll, B., Jayawardhana, R., Fortney, J. J., Lafrenière, D., & Albert, L. 2010, ApJ, 718, 920
Croll, B., Lafreniere, D., Albert, L., et al. 2011, AJ, 141, 30
Crossfield, I. J. M., Barman, T., & Hansen, B. M. S. 2011, ApJ, 736, 132
Crossfield, I. J. M., Hansen, B. M. S., & Barman, T. 2012, ApJ, 746, 46
Cushing, M. C., Rayner, J. T., & Vacca, W. D. 2005, ApJ, 623, 1115
Daemgen, S., Hormuth, F., Brandner, W., et al. 2009, A&A, 498, 567
de Mooij, E. J. W., & Snellen, I. A. G. 2009, A&A, 493, L35
Deming, D., Brown, T. M., Charbonneau, D., Harrington, J., & Richardson, L. J. 2005, ApJ, 622, 1149
Desidera, S., & Barbieri, M. 2007, A&A, 462, 345
Duquennoy, A., & Mayor, M. 1991, A&A, 248, 485
Eastman, J., Siverd, R., & Gaudi, B. S. 2010, PASP, 122, 935
Fabrycky, D., & Tremaine, S. 2007, ApJ, 669, 1298
Foreman-Mackey, D., Hogg, D. W., Lang, D., & Goodman, J. 2012, arXiv:1202.3665
Fortney, J. J., Marley, M. S., & Barnes, J. W. 2007, ApJ, 659, 1661
Fortney, J. J., Shabram, M., Showman, A. P., et al. 2010, ApJ, 709, 1396
Fossati, L., Haswell, C. A., Froning, C. S., et al. 2010, ApJ, 714, L222
Gu, P.-G., Lin, D. N. C., & Bodenheimer, P. H. 2003, ApJ, 588, 509
Hebb, L., Collier-Cameron, A., Loeillet, B., et al. 2009, ApJ, 693, 1920
Hinkle, K. H., Wallace, L., & Livingston, W. 2003, BAAS, 35, 1260
Husnoo, N., Pont, F., Hébrard, G., et al. 2011, MNRAS, 413, 2500
Ibgui, L., Spiegel, D. S., & Burrows, A. 2011, ApJ, 727, 75
Ichikawa, T., Suzuki, R., Tokoku, C., et al. 2006, Proc. SPIE, 6269, 626916
Jefferies, S. M., & Christou, J. C. 1993, ApJ, 415, 862
Jenkins, J. M., Caldwell, D. A., & Borucki, W. J. 2002, ApJ, 564, 495
Katsuno, Y., Ichikawa, T., Asai, K., et al. 2003, Proc. SPIE, 4841, 271
Kleinmann, S. G., & Hall, D. N. B. 1986, ApJS, 62, 501
Knutson, H. A., Charbonneau, D., Cowan, N. B., et al. 2009, ApJ, 690, 822
Kraus, A. L., & Hillenbrand, L. A. 2007, AJ, 134, 2340
Li, S.-L., Miller, N., Lin, D. N. C., & Fortney, J. J. 2010, Nature, 463, 1054
López-Morales, M., Coughlin, J. L., Sing, D. K., et al. 2010, ApJ, 716, L36
Lord, S. D. 1992, A New Software Tool for Computing Earth's Atmospheric Transmission of Near- and Far-infrared Radiation, Technical Report
Luhman, K. L., & Mamajek, E. E. 2010, ApJ, 716, L120
Maciejewski, G., Errmann, R., Raetz, S., et al. 2011, A&A, 528, A65
Madhusudhan, N., Harrington, J., Stevenson, K. B., et al. 2011, Nature, 469, 64
Madhusudhan, N., & Seager, S. 2010, ApJ, 725, 261
Mandell, A. M., Drake Deming, L., Blake, G. A., et al. 2011, ApJ, 728, 18
Mason, B. D., Wycoff, G. L., Hartkopf, W. I., Douglass, G. G., & Worley, C. E. 2001, AJ, 122, 3466
McLean, I. S., Becklin, E. E., Bendiksen, O., et al. 1998, Proc. SPIE, 3354, 566
Miller-Ricci Kempton, E., & Rauscher, E. 2012, ApJ, 751, 117
Montalto, M., Santos, N. C., Boisse, I., et al. 2011, A&A, 528, L17
Nagasawa, M., Ida, S., & Bessho, T. 2008, ApJ, 678, 498
Nymeyer, S., Harrington, J., Hardy, R. A., et al. 2011, ApJ, 742, 35
O'Donovan, F. T., Charbonneau, D., Harrington, J., et al. 2010, ApJ, 710, 1551
Press, W. H. (ed.) 2002, Numerical Recipes in C++ : The Art of Scientific Computing
Rayner, J. T., Toomey, D. W., Onaka, P. M., et al. 2003, PASP, 115, 362
Redfield, S., Endl, M., Cochran, W. D., & Koesterke, L. 2008, ApJ, 673, L87
Rodler, F., Lopez-Morales, M., & Ribas, I. 2012, ApJ, 753, L25
Rogers, J. C., Apai, D., López-Morales, M., Sing, D. K., & Burrows, A. 2009, ApJ, 707, 1707
Schoedel, R., Yelda, S., Ghez, A., et al. 2011, arXiv:1110.2261
Schweitzer, A., Hauschildt, P. H., & Baron, E. 2000, ApJ, 541, 1004
Seager, S. (ed.) 2011, Exoplanets (Tucson, AZ: Arizona Univ. Press)
Seager, S., & Sasselov, D. D. 2000, ApJ, 537, 916
Skrutskie, M. F., Cutri, R. M., Stiening, R., et al. 2006, AJ, 131, 1163
Snellen, I. A. G., de Kok, R. J., de Mooij, E. J. W., & Albrecht, S. 2010, Nature, 465, 1049
Stevenson, K. B., Harrington, J., Nymeyer, S., et al. 2010, Nature, 464, 1161
Suzuki, R., Tokoku, C., Ichikawa, T., et al. 2008, PASJ, 60, 1347
Swain, M., Deroo, P., Tinetti, G., et al. 2012, arXiv:1205.4736
Swain, M. R., Deroo, P., Griffith, C. A., et al. 2010, Nature, 463, 637
Tokunaga, A. T., Simons, D. A., & Vacca, W. D. 2002, PASP, 114, 180
Torres, G., Andersen, J., & Giménez, A. 2010, A&AR, 18, 67
Vacca, W. D., Cushing, M. C., & Rayner, J. T. 2004, PASP, 116, 352
Winn, J. N. 2010, in Exoplanets, ed. S. Seager (Tucson, AZ: Arizona Univ. Press), chapter 4 (arXiv:1001.2010)
Winn, J. N., Holman, M. J., Torres, G., et al. 2008, ApJ, 683, 1076
Yelda, S., Lu, J. R., Ghez, A. M., et al. 2010, ApJ, 725, 331
Zacharias, N., Urban, S. E., Zacharias, M. I., et al. 2004, AJ, 127, 3043
Zhao, M., Monnier, J. D., Swain, M. R., Barman, T., & Hinkley, S. 2012, ApJ, 744, 122